Available online at www.sciencedirect.com
SCIENCE DIRECT®
International Journal of Solids and Structures 43 (2006) 3723–3738
INTERNATIONAL JOURNAL OF SOLIDS and STRUCTURES
www.elsevier.com/locate/ijsolstr

A numerical investigation into the behavior of ground-supported concrete silos filled with saturated solids

Mohamed T. Abdel-Fattah [a], Ian D. Moore [b,*], Tarek T. Abdel-Fattah [c]

[a] *Construction Research Institute, National Water Research Centre, Kanater, Cairo 13621, Egypt*
[b] *GeoEngineering Centre at Queen's—RMC, Queen's University at Kingston, Ont., Canada K7L 3N6*
[c] *Department of Soil Mechanics and Foundation Engineering, Housing and Building Research Centre, Cairo 11511, Egypt*

Received 31 May 2005
Available online 2 August 2005

Abstract

This paper introduces a finite-element solution for simulating the filling process of ground-supported concrete silos filled with saturated granular material. An elasto-plastic axisymmetric finite-element model is used to represent both the granular material and the concrete silo. The interaction between the two materials is modeled using interface elements to allow for relative movement. The filling process is idealized via a multi-stage numerical technique capable of representing both undrained and drained conditions for the granular material. The effects of the relative stiffness between the foundation and wall are examined, as are the boundary conditions at the top of the structure (the roof details).

Depending on the drainage properties of the stored material, the effect of the filling process may be time-dependent. The excess pore water pressure resulting from the filling process may cause a substantial increase in the hoop stresses in the wall. The predicted internal forces may be influenced by the foundation rigidity, but not by the boundary condition at the top of the wall.

The results of these analyses may be used to design experiments to evaluate existing silos, or to develop filling strategies to minimize loads on existing structures.

Keywords: Silo filling; Finite-element analysis; Elasto-plastic model; Consolidation; Foundation rigidity; Boundary conditions

* Corresponding author. Tel.: +1 613 533 3160; fax: +1 613 533 2128.
E-mail address: moore@civil.queensu.ca (I.D. Moore).

0020-7683/$ - see front matter © 2005 Elsevier Ltd. All rights reserved.
doi:10.1016/j.ijsolstr.2005.06.004

Nomenclature

c	cohesion
d	foundation depth
E	Young's modulus
f	stress function
G	shear modulus
H	height
K	pressure ratio
k	coefficient of permeability
M	bending moment in wall
m	power of stress-dependency of bulk solid material stiffness
N	membrane force in wall
P	pressure
q	deviatoric stress
R	strength factor
r	silo radius
T	time
t	thickness
y	depth measured from top of silo
δ	interface displacement
ε	strain
φ	angle of internal friction
ψ	angle of dilatancy
v	Poisson's ratio
γ	unit weight
σ	stress
μ	coefficient of friction between bulk solid and silo wall

1. Introduction

The static pressure induced by a stored material on a silo wall is a significant component of the critical load combination, which may also include dynamic forces due to loading or unloading, thermal effects, and seismic or wind loads. The dynamic effect may be incorporated in the loading combination by multiplying the static pressure by an amplification factor (Hatfield and Bartali, 1988). The present study focuses on the static loading on silo walls during and after silo filling.

Silo walls are primarily subjected to hoop (circumferential) tension due to the pressure exerted by the bulk solids on the wall, and axial (meridianal) compression due to the friction mobilized at the interface, in addition to the wall self-weight. They may also be subjected to meridianal and circumferential bending moments, and radial shear forces. This is dependent on the pressure pattern (symmetric or non-symmetric) to which the wall is subjected and/or the wall boundary conditions. Two general approaches for the analysis and design of silo walls exist (Abdel-Sayed et al., 1985). In the first approach, the pressure induced by the bulk solids on the wall is established with no account for the interaction between the two materials. In the second approach, the composite system of the ensiled material and wall is regarded as a continuum discretized by a number of finite elements connected at their common nodes. The first approach is still widely accepted amongst silo designers, whereas the second one largely restricted to

research purposes. This is perhaps due to the fact that the former is adopted by most silo design codes in which the lateral pressures on the wall are established using either of the two classic silo theories, namely Janssen's theory (1895) and the Reimberts' theory (1976), as alternatives to the determination of the theoretical pressures. Janssen's theory is preferred in the United States of America, while the Reimberts' one is preferred in some parts of Europe (Briassoulis, 1991). The two theories differ fundamentally in the assumption adopted for calculating the pressure ratio (ratio of horizontal to vertical pressures), where this ratio is assumed to be constant in Janssen's theory, but to decrease with depth in the Reimberts' theory. Yet, the pressure ratio together with the bulk solid unit weight are assumed to increase with depth in the specialized version of Janssen's theory (Cowin, 1979). Briassoulis (1991) reported that both theories are unconditionally applicable to any silo geometry and stored material, but showed that the Reimberts' theory overestimates the lateral pressures compared to Janssen's theory. His numerical comparison of the two theories showed that the differences in the pressures obtained from both theories may range from 25% to 95% for elevation ratios ($y/2r$) up to 1, but they become less important for higher elevation ratios. These differences are also dependent on the silo geometry (deep or shallow) and stored material characteristics.

Janssen's silo theory (1895) has constituted the basis for silo design for many decades. This theory accounts for the arching effect within the bulk solids and allows for transfer of part of their weight to the wall as axial compression. It suggests that the horizontal pressure is given by

$$P = \frac{\gamma_s r(1 - e^{-2K\mu y/r})}{2\mu} \tag{1}$$

in which $K =$ ratio of horizontal to vertical pressures, usually assumed equal to Rankine's coefficient of active earth pressure (e.g., Gaylord and Gaylord, 1984; Gurfinkel, 1979)

$$K = \frac{1 - \sin\varphi}{1 + \sin\varphi} \tag{2}$$

Experimental studies on deep silos (Pieper and Wenzel, 1964) have shown that Janssen's Silo Theory could lead to better results by calculating the coefficient K as

$$K = 1 - \sin\varphi \tag{3}$$

equivalent to the coefficient for 'at rest' (zero lateral strain) condition. This naturally leads to higher pressures on the silo wall. Furthermore, Briassoulis (1991) reported that many investigator (e.g., Cowin, 1979; Dabrowski, 1985) had shown analytically that K is bounded by

$$\frac{1 - \sin\varphi}{1 + \sin\varphi} < K < 1 \tag{4}$$

and therefore Eq. (2) merely represents a lower bound for the pressure ratio K.

As a step towards defining more realistic rigorously-based pressure distributions on silo walls, Ooi et al. (1990) measured both the filling and discharge pressures on a prototype tall concrete silo storing barely. These measurements were then used to find the best fitted Janssen pressure distribution from which the wall friction coefficient and lateral pressure ratio were established. The statistical analyses of the eight experiments conducted in the same prototype silo showed that the design storing pressures may be 50% higher than the Janssen values based on the experimental best-fit bulk solid properties. It was also concluded that most silo codes tend to consistently overestimate the wall friction coefficient (an unconservative practice), and may partly compensate by overestimating the lateral pressure ratio (a conservative practice). Nevertheless, this is greatly dependent on the silo geometry (squat or tall silo). Squatter silos may be penalized since their design is sensitive to the lateral pressure ratio, whereas tall ones may be favored because their design is sensitive to the values of the wall friction coefficient.

Because of the potential development of unsymmetrical pressures due to the stored material, a free (patch) load acting on any part of the silo wall may be considered. This approach has been adopted by a number of codes of practice (e.g., DIN 1055; Eurocode EN 1991-4). These unsymmetrical pressures may be unavoidable even in axisymmetric silos with concentric filling, since they may arise as a result of geometric imperfections in the wall and probabilistic changes in the bulk solid properties (Briassoulis, 1998). Using the non-symmetric pressure distributions measured by Ooi et al. (1990), Briassoulis (1998) conducted a finite-element analysis for the shell structure to establish the state of stress in the shell. The results obtained from his analyses suggested that the design of silo walls might not neglect the asymmetric features of the real pressures developed by the stored material. However, the effect of the non-symmetric pressure is not considered here since it is out of the scope of this investigation.

Another aspect of silo design also requires consideration, namely the behavior of wet silage and the potential effects of consolidation during or after the filling process. Design standards like the National Farm Building Code of Canada (1995) require any zone of saturated silage to be identified, and silo wall pressures to include explicit consideration of hydrostatic pressures acting against the wall in the zone of saturated material at the base of the silo. This generally makes a very substantial contribution to the lateral wall pressures, and can lead to much greater wall strength requirements. Design of "Class II" structures (those expected to hold wet silage), requires assessment of lateral pressures associated with high filling speed, neglecting any influence of "primary consolidation" of the ensiled material (reductions in pore water pressure as water drainage leads to compression of that material). Consolidation may actually occur, so that lateral pressures and the wall thicknesses required may depend on the speed with which the silo can be filled. An understanding of the loading speed and the effect of silage consolidation is investigated in this paper, using numerical simulations of the filling process to estimate the forces that develop in a ground-supported concrete silo filled with saturated material. Calculations are performed assuming that the filling process is completed over a predefined number of stages; with consolidation allowed following completion of each stage. Accordingly, the number and frequency (time elapsed between) of the filling stages are expected to affect the patterns of forces developed in the structure, given the reoccurring pattern of development and dissipation of the excess pore pressure within the bulk solid. For consolidating silage, the structure must be designed to withstand the temporary forces developed due to the undrained conditions, where out-of-equilibrium water pressures may exceed those due to silage in a drained (consolidated) condition.

One particular silo geometry (height 10 m, radius 5 m, and wall thickness 0.15 m) is used here to examine the effects on the forces developed in the structure as a result of silage consolidation, the stiffness of the foundation relative to the wall, as well as the top boundary conditions (those relating to the roof system used over the structure).

2. Geometric and material properties

Fig. 1 displays the geometric properties of the example ground-supported concrete silo. Unless specified otherwise, the proposed silo geometry has the following properties: radius $r = 5.0$ m; height $H = 10.0$ m; height of ensilage $H_e = 9.0$ m; height of conical surcharge $H_{sur} = 0.0$ m; wall thickness $t_w = 0.150$ m; foundation thickness $t_f = 0.45$ m; foundation depth $d = 1.0$ m. This silo geometry is not proposed as an adequate design. Concrete is modeled with Young's modulus $E_c = 20.0$ GPa, and Poisson's ratio $v_c = 0.20$.

For the foundation and wall, an elasto-plastic model is used, but the results obtained show that the stresses in concrete would remain in the elastic range.

For the saturated granular material and the foundation soil, the same material-hardening constitutive model (Schanz, 1998) adopted by the Finite-Element code PLAXIS (Brinkgreve and Vermeer, 1998) is used. A detailed description for this model is given in the PLAXIS User's Manual, but for convenience the essentials of this model are presented here. The hardening-soil model is an advanced model for simu-

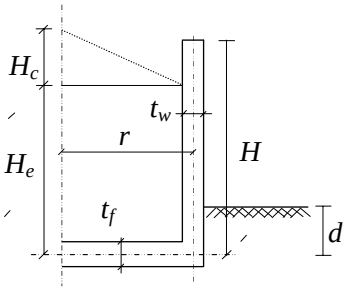

Fig. 1. Geometry of the ground-supported concrete silo.

lating the behavior of both soft and stiff soils. As a hardening plastic model, it has a yield surface that is not fixed in the principal stress space. Both shear hardening and compression hardening are represented in the model. The basic assumption in the model formulation is that the relationship between the vertical strain ε_1 and the deviatoric stress q in the primary triaxial loading can be approximated by a hyperbola as shown in Fig. 2. Such a relationship was first formulated by Kondner (1963), and used subsequently in the well-known hyperbolic model (Duncan and Chang, 1970).

The hyperbolic relationship plotted in Fig. 2 can be described by

$$-\varepsilon_1 = \frac{1}{2E_{50}} \frac{q}{1 - q/q_a}, \quad \text{for } q < q_f \tag{5}$$

where E_{50} is a confining-stress-dependent stiffness modulus for primary loading, and q_f and q_a are, respectively, the ultimate and asymptotic deviatoric stresses which can be obtained from the relations

$$q_f = (c \cot \varphi - \sigma'_3) \frac{2 \sin \varphi}{1 - \sin \varphi} \tag{6}$$

and

$$q_a = q_f / R_f \tag{7}$$

where R_f a failure ratio that should be smaller than unity, and σ'_3 is the confining pressure in a triaxial test. The stiffness modulus E_{50} is given by

$$E_{50} = E_{50}^{ref} \left(\frac{c \cot \varphi - \sigma'_3}{c \cot \varphi + p^{ref}} \right)^m \tag{8}$$

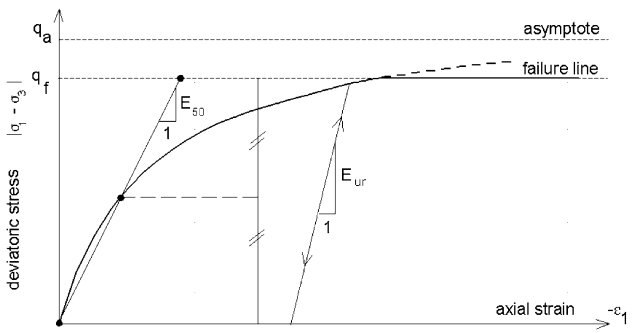

Fig. 2. Hyperbolic stress–strain relation in primary loading for a standard drained triaxial test (adapted from PLAXIS User's Manual 1998).

where E_{50}^{ref} is a reference stiffness modulus corresponding to the reference confining pressure p^{ref}, and m is the power of stress-level dependency of stiffness that is normally assumed to have values around 0.50 for sands and silts as reported by Janbu (1963).

For unloading and reloading stress paths, the model uses another stress-dependent stiffness modulus defined by

$$E_{\text{ur}} = E_{\text{ur}}^{\text{ref}} \left(\frac{c \cot \varphi - \sigma_3'}{c \cot \varphi + P^{\text{ref}}} \right)^m \tag{9}$$

where $E_{\text{ur}}^{\text{ref}}$ is the reference stiffness modulus for unloading and reloading corresponding to the reference confining pressure p^{ref}, normally taken equal to $3E_{50}^{\text{ref}}$ in many practical situations as cited in PLAXIS User's Manual (Brinkgreve and Vermeer, 1998). The Oedometer stiffness E_{oed} for one-dimensional compression is defined by

$$E_{\text{oed}} = E_{\text{oed}}^{\text{ref}} \left(\frac{c \cot \varphi - \sigma_1'}{c \cot \varphi + P^{\text{ref}}} \right)^m \tag{10}$$

where $E_{\text{oed}}^{\text{ref}}$ is a tangent stiffness at a vertical stress of $-\sigma_1' = P^{\text{ref}}$.

The model's yield function is defined by

$$f = \bar{f} - \gamma^{\text{p}} \tag{11}$$

where $\bar{f}$ is a function of stress given by

$$\bar{f} = \frac{1}{E_{50}} \frac{q}{1 - q/q_{\text{a}}} - \frac{2q}{E_{\text{ur}}} \tag{12}$$

and γ^{p} is a function of plastic strains defined by

$$\gamma^{\text{p}} = -(2\varepsilon_1^{\text{p}} - \varepsilon_{\text{v}}^{\text{p}}) \approx -2\varepsilon_1^{\text{p}} \tag{13}$$

in which ε_1^{p} and $\varepsilon_{\text{v}}^{\text{p}}$ are, respectively, the axial and volumetric plastic strains. For primary loading where $\gamma^{\text{p}} = \bar{f}$,

$$-\varepsilon_1^{\text{p}} \approx \frac{1}{2}\bar{f} = \frac{1}{2E_{50}} \frac{q}{1 - q/q_{\text{a}}} - \frac{q}{E_{\text{ur}}} \tag{14}$$

The elastic strains that develop during both primary loading and unloading/reloading are defined by

$$-\varepsilon_1^{\text{e}} = \frac{q}{E_{\text{ur}}}; \quad -\varepsilon_2^{\text{e}} = -\varepsilon_3^{\text{e}} = -\nu_{\text{ur}} \frac{q}{E_{\text{ur}}} \tag{15}$$

where ν_{ur} is the unloading/reloading Poisson's ratio.

From Eqs. (14) and (15), the axial strain in the deviatoric stage of the triaxial test can be written as

$$-\varepsilon_1 = -\varepsilon_1^{\text{e}} - \varepsilon_1^{\text{p}} \approx \frac{1}{2E_{50}} \frac{q}{1 - q/q_{\text{a}}} \tag{16}$$

The relation between the rates of plastic shear strain and plastic volumetric strain is governed by the flow rule

$$\dot{\varepsilon}_{\text{v}}^{\text{p}} = \sin \psi_{\text{m}} \dot{\gamma}^{\text{p}} \tag{17}$$

where ψ_{m} is the mobilized angle of dilatancy defined by

$$\sin \psi_{\text{m}} = \frac{\sin \varphi_{\text{m}} - \sin \varphi_{\text{cv}}}{1 - \sin \varphi_{\text{m}} \sin \varphi_{\text{cv}}} \tag{18}$$

in which φ_{cv} is the critical state friction angle, and φ_m is the mobilized friction angle defined by

$$\sin\varphi_m = \frac{\sigma'_1 - \sigma'_3}{\sigma'_1 + \sigma'_3 - 2c\cot\varphi} \tag{19}$$

The critical state friction angle can be obtained by replacing the mobilized friction and dilatancy angles in Eq. (18) by their values at failure (φ and ψ), and hence

$$\sin\varphi_{cv} = \frac{\sin\varphi - \sin\psi}{1 - \sin\varphi\sin\psi} \tag{20}$$

The present study is carried out assuming that the example silo is filled with saturated sand, a material used previously by many investigators (e.g., Briassoulis, 1991; Holst et al., 1999) in silo loading studies. The material parameters assigned to the saturated sand are assumed to be as follows:

$$E_{50}^{ref} = 1.2\times10^5\ \text{kN/m}^2;\quad E_{oed}^{ref} = 1.33\times10^5\ \text{kN/m}^2;\quad E_{ur}^{ref} = 3.6\times10^5\ \text{kN/m}^2;$$
$$v_{ur} = 0.20;\quad P^{ref} = 200\ \text{kN/m}^2;\quad \varphi = 33^\circ;\quad \psi = 3^\circ;\quad m = 0.50;\quad \gamma_d = 17\ \text{kN/m}^3;$$
$$\gamma_{wt} = 21\ \text{kN/m}^3;\quad k_x = k_y = 0.50\ \text{m/day};\quad c^{ref} = 1.0\ \text{kN/m}^2$$

While the foundation soil could be modeled as different to the ensiled material, the use of the same material is a simple choice that is adequate for this first study of time-dependent filling and the other factors outlined earlier.

3. Finite-element model

3.1. Description of the model and procedure

An axisymmetric finite-element model is used to represent the concrete silo and the saturated granular material (sand), as well as the foundation soil. The silo wall is modeled using 3-noded beam elements, whereas the solids are modeled using 6-noded triangular solid elements. A typical finite-element mesh is shown in Fig. 3. The model is restrained in the horizontal direction at the axis of symmetry and the soil

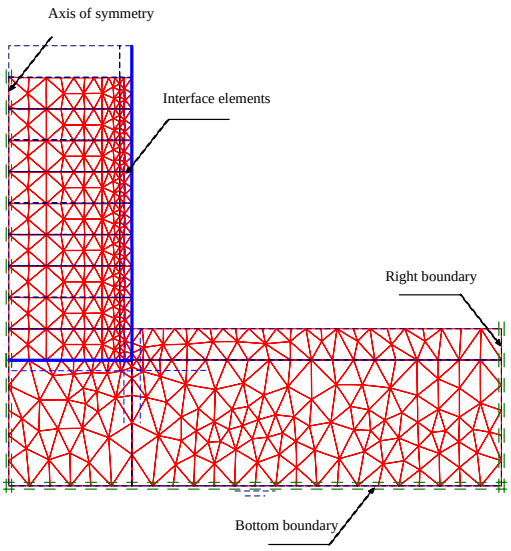

Fig. 3. A typical finite-element mesh.

right-hand boundary, whereas it is prevented from vertical movement at its lower boundary. In addition, the wall is restrained in the radial direction at its top. Closed consolidation boundaries are imposed at the axis of symmetry, beneath the foundation, and at the right-hand boundary, where there is zero flow of water normal to the surface. For the foundation soil, a fully drained condition is assumed.

The interaction between the silo wall and bulk solids is modeled using interface elements. The use of these elements permits modeling of an interface condition between the smooth (no friction) and the rough (full compatibility) limits. A strength factor R_{int} is introduced to define the strength parameters of the interface relative to those of the original material, thus,

$$c_{\text{int}} = R_{\text{int}} \times c_{\text{s}} \tag{21a}$$

$$\tan\varphi_{\text{int}} = R_{\text{int}} \times \tan\varphi_{\text{s}} \tag{21b}$$

$$G_{\text{int}} = R_{\text{int}}^2 \times G_{\text{s}} \leqslant G_{\text{s}} \quad \text{and} \tag{21c}$$

$$E_{\text{oed,int}} = 2G_{\text{int}} \frac{1 - \nu_{\text{int}}}{1 - 2\nu_{\text{int}}} \tag{21d}$$

where the Poisson's ratio for the interface material $\nu_{\text{int}} = 0.45$.

Throughout this investigation, a value of 0.70 is assigned to the strength factor R_{int}, a typical value for the strength parameter of a sand–concrete interface.

Fig. 4 shows the connectivity of the interface element to the 6-noded axisymmetric element. In Fig. 4, the element has a virtual thickness t_{int}, but in the finite-element formulation the coordinates of the reciprocal nodes are coincident. The virtual thickness may be established by multiplying the average element size by a virtual thickness factor. It is used to calculate the magnitudes of the interface displacements (gap and slip displacements) when the interface behaves elastically as follows:

$$\delta_{\text{g}} = \frac{\sigma t_{\text{int}}}{E_{\text{oed,int}}} \tag{22a}$$

and

$$\delta_{\text{sl}} = \frac{\tau t_{\text{int}}}{G_{\text{int}}} \tag{22b}$$

It is clear from Eq. (22) that large displacements may occur if very low values are assigned to the interface element elastic parameters, whereas numerical "ill-conditioning" may result if very high values are assigned to these parameters; and this is also obviously dependent on the value assigned to the virtual thickness.

Therefore, the sensitivity of the obtained results, listed in Table 1, to the assumed virtual thickness has been examined. The internal forces in the wall were established due to virtual thicknesses of 0.05, 0.10, 0.20,

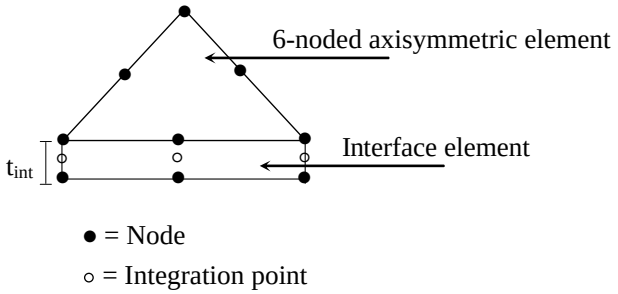

Fig. 4. Connectivity of the interface element to the 6-noded axisymmetric element.

Table 1
Internal forces due to different virtual thicknesses

Internal force	Virtual thickness			
	$\delta = 0.05$	$\delta = 0.10$	$\delta = 0.20$	$\delta = 0.30$
N_ϕ (kN/m)	125.50	121.80	113.50	106.10
N_θ (kN/m)	270.4	264.10	255.70	245.40
Q_r (kN/m)	8.88	9.46	9.90	9.56
M_ϕ (kN m/m)	9.21	8.95	8.45	7.85

and 0.30, respectively. From Table 1, it can be noticed that the internal forces increases as the virtual thickness decreases, and thus assigning a low value to this thickness may be regarded as a conservative practice. In fact, the choice of the proper value of the virtual thickness should be made in the light of compiled experimental data. However, based on the fact that the results obtained from the present study only concern a structure with the geometric and material properties assumed here, throughout this investigation, a default value of 0.1 is assigned to this factor, since no measurements are available at this early stage of the investigation.

The filling process is simulated in the finite-element model via a multi-step analysis strategy, with the ensiled material placed in a number of layers of constant thickness.

3.2. Comparison with a closed-form solution

Hatfield and Bartali (1988) introduced a closed-form solution for the static forces and moments in a grain silo. The proposed silo material is homogenous, isotropic and linearly elastic, and the wall thickness is small compared to the radius. The silo is full of grain but not heaped ($H_{sur} = 0.0$). Horizontal grain pressure, P, is given by Janssen's formula (Eq. (1)). The above assumptions result in axially symmetric forces and deformations. These forces are the hoop force N_θ, meridianal force N_ϕ; radial shear Q_r, and meridianal moment M_ϕ.

An example silo, with the properties examined by Hatfield and Bartali (1988), was analyzed using the above solution: height $H = 15.0$ m, radius $r = 3.0$ m, and wall thickness $t_w = 0.155$ m. The wall material has a Young's modulus $E_w = 25.0$ GPa, Poisson's ratio $v_w = 0.30$, and unit weight $\gamma_w = 24$ kN/m^3. The grain properties are $\gamma_s = 8.0$ kN/m^3, $K = 0.31$, and $v_s = 0.40$. This structure is taller than that examined in the study of silage consolidation that is the principal focus of this paper, so it assesses whether the finite-element analysis can reproduce the full Janssen arching behavior.

The internal forces in the wall were obtained for different boundary conditions at the bottom edge of the silo. A comparison between the results obtained from both the closed-form solution and the present finite-element solution for the limiting case of zero restraint is shown in Fig. 5. From Fig. 5a, it can be seen that Janssen's theory underestimates the wall pressure, and this becomes more pronounced near to the silo base. This may partly be attributed to the fact that the ratio of the horizontal to vertical pressures varies with depth; this ratio is assumed constant in the closed-form Janssen solution. The finite-element solution predicts a sharp increase in the pressure along the lower fifth of the silo height. At the silo base, an increase in the pressure of 45% is predicted. The same observations may be made from Fig. 5b and c which present, respectively, the hoop and axial force distributions along the silo height.

For the other limiting case of infinitely stiff restraint (radial displacement and rotation are prevented) at the bottom edge of the silo, the maximum magnitudes of the hoop force and meridianal bending moment in the wall obtained from both solutions are listed in Table 2. In Table 2, the positive sign for the bending moment indicates that the wall outer fiber is subjected to tensile bending stresses. The maximum negative bending moment occurs at the wall bottom edge. It can be seen from Table 2 that the finite-element results

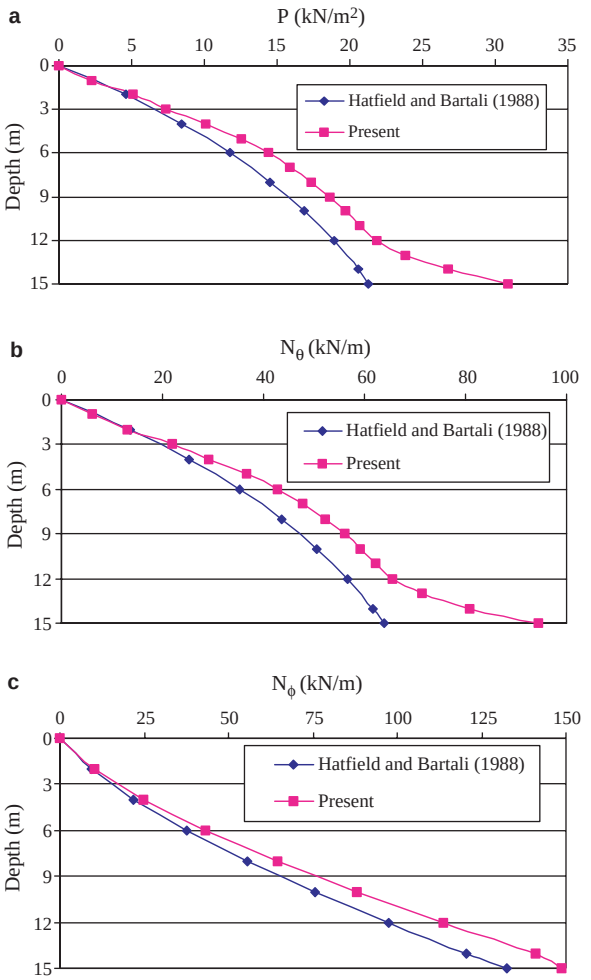

Fig. 5. Results obtained from the closed-form and FE solutions: (a) wall pressure distribution, (b) hoop force distribution, and (c) axial force distribution.

Table 2
Internal forces obtained from the analytical and finite-element solutions

Maximum internal force	Solution	
	Analytical	Finite-element
Tensile N_θ (kN/m)	65.0	79.0
Compressive N_θ (kN/m)	−40.0	−47.50
Positive M_ϕ (kN m/m)	1.0	1.23
Negative M_ϕ (kN m/m)	−5.0	6.0

are about 20–23% higher than their analytical counterparts. The location of the maximum hoop tension estimated from the analytical solution is 1.6 m from the silo base whereas that estimated from the finite-element solution is 1.45 m from the silo base.

It is to be noted that the differences between the results obtained from both solutions are expected since Janssen's theory, based on which the analytical solution was formulated, has been shown to be inaccurate and unconservative (Abdel-Sayed et al., 1985; Bishara et al., 1983).

4. Results of analyses and discussion

Four filling schemes are examined here. These represent, filling configurations composed of, one layer, two layers, three layers, and five layers respectively. For filling schemes 2 and 3, the height H_e (9.0 m) is equally divided into two and three layers, respectively. For filling scheme 4, the height H_e is divided into four layers each of 2.0 m thickness, and a top layer of 1 m thickness.

The results obtained via both undrained and drained conditions are shown in Figs. 6–8.

Fig. 6 shows the maximum axial (meridianal) load in the wall for the four filling schemes. This maximum axial load occurs at the wall bottom edge. The general trend in Fig. 6 is that the axial load in the wall is higher for the drained condition. This is due to the increase in the relative vertical movement between the ensiled material and the wall at the interface, resulting from the settlement of the ensiled material due to consolidation. It can also be seen that the axial load associated with the undrained condition is higher when there is a greater number of filling layers. For instance, the axial load predicted due to filling scheme 4 (5 layers) is approximately two and half times that predicted due to filling scheme 1 (1 layer). This is because the excess pore water pressure developed in each specific layer is permitted to entirely dissipate prior to adding the subsequent one. Thus, the one-step-filling scheme (scheme 1) is characterized by the development of maximum pore water pressure, and consequently minimum axial load in the wall.

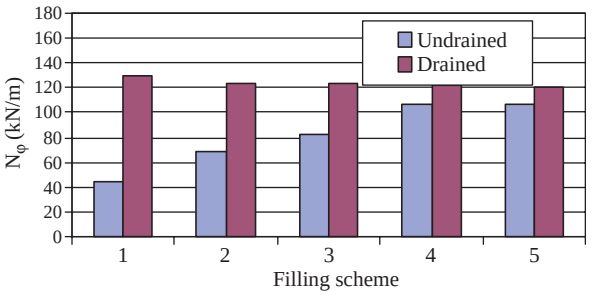

Fig. 6. Undrained and drained axial forces in the wall due to the four filling schemes.

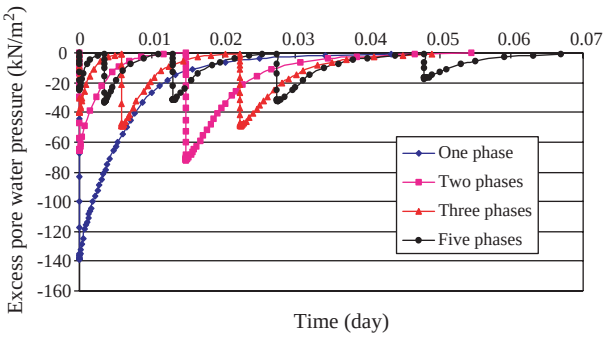

Fig. 7. Variation of the excess pore water pressure with time.

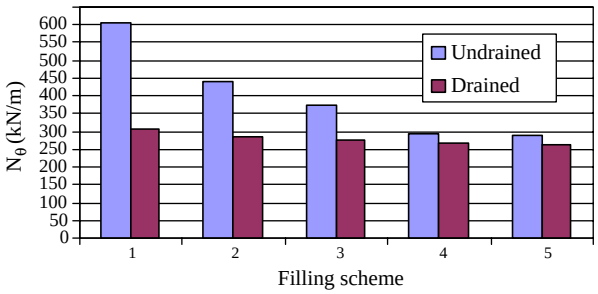

Fig. 8. Undrained and drained hoop forces in the wall due to the four filling schemes.

The variation of the excess pore pressure with time is plotted in Fig. 7 for a point which lies in the middle of the bottom layer. In Fig. 7, at time $T = 0.0$ (assuming a rapid filling process) a maximum excess pore water pressure of about 140 kN/m^2 is predicted due to filling scheme 1. On the other hand, a minimum excess pore water pressure of about 20 kN/m^2 is predicted due to filling scheme 4. The estimated time for dissipation of the excess pore pressure is about 60 min and 98 min for filling schemes 1 and 4, respectively. The former is associated with one period following complete filling, whereas the latter is associated with five time intervals following the corresponding filling stages.

Fig. 8 plots the maximum hoop forces in the wall due to both the undrained and drained conditions for the four filling schemes. The general trend in Fig. 8 is that the hoop force in the wall is higher for the undrained condition since it is directly proportional to the internal pressure in the stored material. The latter increases as the excess pore water pressure increases. The predicted hoop force due to one-step filling (scheme 1) is approximately two and half times that predicted due to the five-step filling scheme (scheme 4). This is because dissipation of the excess pore pressure, prior to adding each subsequent layer, occurs for scheme 4.

Thus, the hoop force in the wall is greatly influenced by excess pore pressure that develops in the ensiled material during filling. In that case, wall design for hoop stresses has to be performed assuming an undrained condition, where the specific stresses depend on the rate of loading (filling). This is not the case while designing the wall for normal stresses, since these stresses are critical for the fully drained condition.

Fig. 9 plots the values of the axial and hoop forces in the foundation at its central point, where these two forces are equal, associated with both the undrained and drained conditions for the four filling schemes. It is evident from Fig. 9 that these values are higher for the undrained condition, again due to the development of excess pore pressure in the ensiled material. The maximum value for the undrained condition

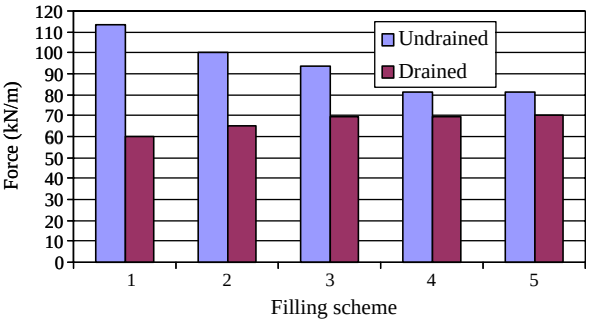

Fig. 9. Distribution of axial and hoop forces in the foundation central point.

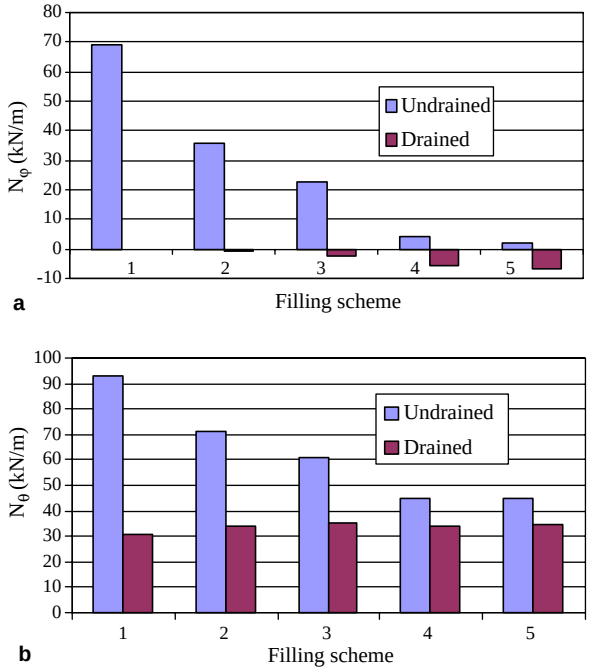

Fig. 10. Distribution of forces in foundation edge: (a) axial force, and (b) hoop force.

occurs for scheme 1 where the largest values of excess pore pressure develop. This value is about 40% higher than that predicted for scheme 4.

The predicted values of the axial and hoop forces in the foundation corner are plotted in Fig. 10a and b, respectively. As with those predicted at the centre of the foundation, these values are higher for the undrained condition. A comparison between Fig. 10a and b reveals that the axial load is more sensitive to the filling rate than the hoop force. For the undrained condition, the values for the axial and hoop forces predicted from scheme 4 are, respectively, about 14 and 2 times those predicted from scheme 1. In Fig. 10a, it appears that the predicted values for the axial load from the drained condition may become compressive as a result of the inward movement of that point.

5. Effect of foundation stiffness

To examine the effect of the relative stiffness between the foundation and wall, the hoop forces in the wall are presented for ratios of foundation to wall thickness t_f/t_w up to 6. The results for both the undrained and drained conditions are displayed in Fig. 11a and b, respectively. In these figures, the forces in the wall corresponding to a specific value of t_f/t_w are normalized with respect to those corresponding to $t_w = t_f = 0.15$ m.

The general trend in these figures is that the hoop force in the wall decreases as the ratio t_f/t_w increases. This becomes more notable as the slenderness ratio r/t_w decreases. For example, as the ratio t_f/t_w increases from 1 to 4, the drained hoop force in the wall drops by 71% and 11% for $r/t_w = 13$ and 133, respectively. In general, the results become insensitive to t_f/t_w once that ratio exceeds 4.

A comparison between Fig. 11a and b shows that the stiffness ratio has somewhat more effect for silage giving drained response, especially for lower slenderness ratios. This likely results because the increase in

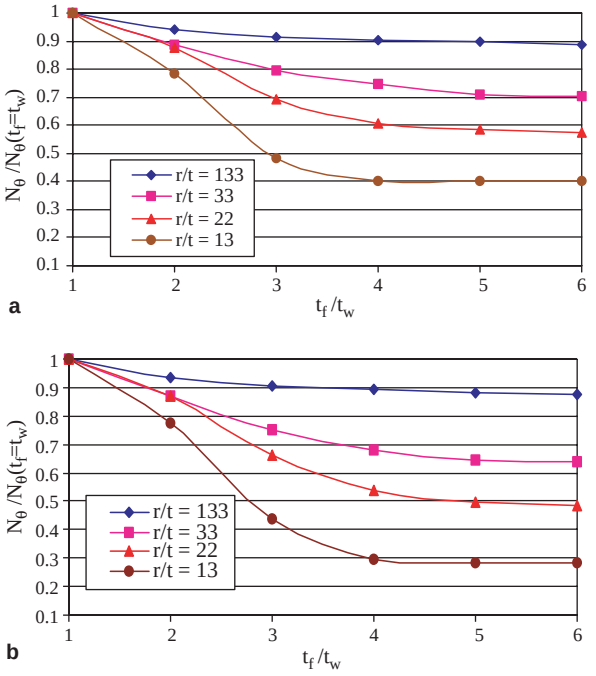

Fig. 11. Effect of the relative stiffness between the foundation and wall on the hoop forces in the wall: (a) undrained condition, and (b) drained condition.

relative stiffness between foundation and wall provides additional restraint to the wall, leading to a reduction in its horizontal (radial) displacement. A reduction in the hoop force in the wall follows.

On the other hand, the analysis indicates that the effect of the relative stiffness between the wall and foundation on the axial wall force is much less pronounced. Generally, the increase in t_f/t_w is associated with a decrease in the axial load, most notably for lower slenderness ratios. Presumably the foundation stiffness leads to a decrease in the vertical displacement of the wall relative to the centre of the ensiled material, and consequently a decrease in the relative vertical movement of the bulk solid relative to the wall, and shear mobilized at the interface.

6. Effect of boundary conditions

The foregoing results were obtained for lateral restraint applied to the wall top. A silo free at its top is considered here to examine the effect of that restraint. The results obtained for these two different boundary

Table 3
Membrane forces in silo wall due to two cases of boundary conditions

r/t_w	Laterally restrained top				Free top			
	$t_f/t_w = 1.0$		$t_f/t_w = 6.0$		$t_f/t_w = 1.0$		$t_f/t_w = 6.0$	
	N_ϕ (kN/m)	N_θ (kN/m)	N_ϕ (kN/m)	N_θ (kN/m)	N_ϕ (kN/m)	N_θ (kN/m)	N_ϕ (kN/m)	N_θ (kN/m)
133	107.0	872.0	119.0	763.0	106.8	872.0	118.50	764.0
13	98.70	210.70	106.90	60.10	98.70	210.70	106.90	60.10

conditions are listed in Table 3. It is clear from Table 3 that the lateral restraint at the top has a negligible effect on the results. This is true for the whole range of slenderness ratios considered, regardless of the relative stiffness between the foundation and wall.

7. Conclusions

A finite-element solution for the internal forces in ground-supported concrete silos due to filling is presented. The results are obtained using an elasto-plastic axisymmetric finite-element model representing the silo structure and stored material, as well as the foundation soil. The silo is filled with a saturated granular material (sand) according to a multi-stage filling process. The results of analyses are obtained due to both undrained and drained conditions.

A number of conclusions may be drawn for the combination of materials, geometry, and loading considered in this investigation. Firstly, the development of excess pore pressure during the filling process may temporarily cause a substantial increase in the hoop stresses in the wall. This makes the filling rate a factor that should be considered during wall design for hoop forces. This time-dependent effect can be minimized if reasonable, practical time intervals are left between the filling stages, so the accumulated pore pressure are allowed to dissipate prior to the commencement of the next filling stage. Indeed, filling with materials having lower permeability will require a longer time interval for dissipation of the pore pressure. Naturally, that time interval should be acceptable from a practical standpoint, considering the operations of the bulk solids handling facility. Otherwise, facility use would need to include undesirable delays to permit dissipation of the pore pressures.

The hoop forces mobilized in the wall are significantly influenced by the relative stiffness between the silo foundation and wall. The hoop force decreases as the foundation becomes stiffer. This effect is particularly pronounced for silos with base thickness nearly equal to wall thickness. By contrast, any increase in the relative stiffness between the silo foundation and wall seems to have a negligible effect on the axial force in the wall, regardless of the silo slenderness.

The lateral restraint at the top of the wall has negligible effect on the forces that develop in the wall, regardless of the foundation rigidity.

The results obtained from this investigation may be useful while planning a field testing program, and may assist during evaluation of existing concrete silos. Following experimental evaluation, the proposed analysis methodology might also be used in concrete silo design.

References

Abdel-Sayed, G., Monasa, F., Siddall, W., 1985. Cold-formed steel farm structures Part I: Grain Bins. Journal of Structural Engineering, American Society of Civil Engineers 111 (10), 2065–2089.

Bishara, A.G., Ayoub, S.F., Mahdy, A.S., 1983. Static pressures in concrete cylinders storing granular materials. Journal of American Concrete Institute 80 (3), 210–216.

Briassoulis, D., 1998. Finite-element analysis of a cylindrical silo shell under unsymmetrical pressure distributions. In: Proceedings of Advances in Civil and Structural Engineering. Civil-Comp Press, Edinburgh, pp. 31–39.

Briassoulis, D., 1991. Limitations in the range of applicability of the classic silo theories. Structural Journal, American Concrete Institute 88 (4), 437–444.

Brinkgreve, R.B.J., Vermeer, P.A., 1998. PLAXIS-version 7, Finite-element code for soil and rock analyses. In: User's Manual. A.A. Balkema, Rotterdam, The Netherlands.

Cowin, S.C., 1979. Pressure ratio in the theory of bin-pressures. Journal of Applied Mechanics 46, 524–528.

Dabrowski, R., 1985. Discussion of design pressures in circular bins. Journal of Structural Engineering, American Society of Civil Engineers 111 (9), 2074–2076.

DIN 1055, 1987. Design loads for buildings: loads in silo containers, Part 6. Deutsches Institut fur Normung, Berlin, Germany.

Duncan, J.M., Chang, C.Y., 1970. Nonlinear analysis of stress and strain in soil. Journal of the Soil Mechanics and Foundations Division, American Society of Civil Engineers 96, 1629–1653.

EN 1991-4, 2004. Eurocode1: basis of design and actions on structures, Part 4—silos and tanks, Eurocode 1. CEN, Brussels.

Gaylord, E.H., Gaylord, C.N., 1984. Design of Steel bins for Storage of Bulk Solids. Prentice-Hall Inc., Englewood Cliffs, p. 359.

Gurfinkel, G., 1979. Reinforced-Concrete Bunkers and Silos. Structural Engineering Handbook, second ed. McGraw-Hill, New York, p. 22.

Hatfield, F.J., Bartali, E., 1988. Static forces and moments in a grain silo. Journal of Structural Engineering, American Society of Civil Engineers 114 (12), 2814–2819.

Holst, J.M.F.G., Ooi, J.Y., Rotter, J.M., Rong, G.H., 1999. Numerical modelling of silo filling. I: Continuum analysis. Journal of Engineering Mechanics, American Society of Civil Engineers 125 (1), 94–103.

Janbu, J., 1963. Soil compressibility as determined by oedometer and triaxial tests. In: Proceedings of the European Conference on Soil Mechanics and Foundation Engineering, Wiesbaden, vol. 1, pp. 19–25.

Janssen, H.A., 1895. Versuche uber Getreidedruck in Silozellen. Zeitschrift des Vereines Deutscher Ingenieure, p. 1045.

Kondner, R.L., 1963. A hyperbolic stress strain formulation for sands. In: Proceedings of the Second Pan. Am. International Conference on Soil Mechanics and Foundation Engineering, Brazil, vol. 1, pp. 289–324.

National Farm Building Code of Canada, 1995. Canadian Commission on Building and Fire codes, Institute for Research in Construction, National Research Council of Canada.

Ooi, J.Y., Pham, L., Rotter, J.M., 1990. Systematic and random features of measured pressures on full-scale silo walls. Journal of Engineering Structures 12 (2), 74–87.

Pieper, K., Wenzel, F., 1964. Pressure Conditions in Silos. W. Ernst and John, Berlin, Germany.

Reimbert, M.L., Reimbert, A.M., 1976. SILOS—Theory and Practice, first ed. Trans Tech Publications, Clausthal-Zellerfeld, p. 251.

Schanz, T., 1998. Zur Modellierung des Mechanischen Verhaltens Von Reibungsmaterialen, Habilitation, Stuttgart Universität, Germany.